MATERIALS SCIENCE

Mesocrystalline calcium silicate hydrate: A bioinspired route toward elastic concrete materials

Andreas Picker,[1]* Luc Nicoleau,[2] Zaklina Burghard,[3] Joachim Bill,[3] Igor Zlotnikov,[4]† Christophe Labbez,[5] André Nonat,[5] Helmut Cölfen[1]‡

Calcium silicate hydrate (C-S-H) is the binder in concrete, the most used synthetic material in the world. The main weakness of concrete is the lack of elasticity and poor flexural strength considerably limiting its potential, making reinforcing steel constructions necessary. Although the properties of C-S-H could be significantly improved in organic hybrids, the full potential of this approach could not be reached because of the random C-S-H nanoplatelet structure. Taking inspiration from a sea urchin spine with highly ordered nanoparticles in the biomineral mesocrystal, we report a bioinspired route toward a C-S-H mesocrystal with highly aligned C-S-H nanoplatelets interspaced with a polymeric binder. A material with a bending strength similar to nacre is obtained, outperforming all C-S-H–based materials known to date. This strategy could greatly benefit future construction processes because fracture toughness and elasticity of brittle cementitious materials can be largely enhanced on the nanoscale.

INTRODUCTION

Calcium silicate hydrate (C-S-H) is the main phase of hydrated cement and the cohesive building block of concrete, the most used human-made material in the world. Although it shows good compressive strength, C-S-H presents a lack of elasticity and a poor flexural strength (*1*). This weakness is traditionally compensated on the macroscopic scale by the use of costly reinforcing steel bars. Today, the most pursued route to enhanced elastic properties is the formation of C-S-H/organic hybrids on the nanoscale by incorporating soft matter into and/or in between the C-S-H nanoplates (*2*–*6*). In addition, fiber-reinforced ultra-high performance concrete and macro-defect-free (MDF) cement were reported with flexural strengths up to 50 to 70 MPa (*7*–*9*). However, in all approaches, the C-S-H nanoplatelets are still randomly aggregated, and thus, the potential mechanical performance remains limited (*10*). Here, we show that a promising, nature-inspired strategy to create elasticity in cementitious systems is the formation of oriented, layered inorganic-organic C-S-H mesocrystals similar to biomaterials like the sea urchin spine (*11*–*13*). Mesocrystals, perfectly aligned over hundreds of micrometers, are obtained in solution from the self-assembly of initially stabilized C-S-H by polymers selected according to previously performed phage display experiments (*14*). These highly oriented C-S-H hybrids present bending strength similar to nacre and nacre-inspired materials (table S1) and outperform all C-S-H–based materials known to date showing the advantage of the mesocrystal structure with aligned C-S-H platelets interspaced with polymeric binder.

Forming mesocrystals usually requires good particle dispersion before they assemble into such an ordered structure. Unfortunately, pure C-S-H suspensions consist of large and loose aggregates because of prominent secondary nucleation and strong attractive forces between particles (*15*, *16*). To hamper the C-S-H platelet aggregation, regular dispersants can be used (*17*, *18*), but perfectly ordered structures require the best possible dispersants to achieve minimal uncontrolled aggregation. For this purpose, three polymers were selected: poly (1-vinylpyrrolidone-co-acrylic acid) (PVP-co-PAA) and two kinds of poly(acrylamide-co-acrylic acid) (PAAm-co-PAA) (chemical structures and specifications shown in fig. S1). This selection arose from a phage display assay (*14*) and simulations (*19*), which suggested two necessary main features for achieving strong specific C-S-H/polymer interactions:

1)negatively charged groups for Ca^{2+}-mediated electrostatic interactions

2)hydrophilic residues preferentially with alcohol or amide groups for hydrogen bond interactions.

RESULTS

To control and monitor the C-S-H precipitation, a titration setup (*20*) was used to add $CaCl_2$ solution into Na_2SiO_3 solution at constant pH 12 or 13 in the presence of the mentioned polymers (Syntheses section in Materials and Methods). Instead of immediate aggregation, the resulting C-S-H particles remain colloidally stable and do not show any agglomeration during at least 3 months, as demonstrated by analytical ultracentrifugation (AUC) measurements (fig. S2).

In the following, the focus will only lie on C-S-H stabilized with PVP-co-PAA, although PAAm-co-PAA gives similar results. The AUC analysis of the colloidal dispersion reveals a predominant hydrodynamic particle diameter of 24 nm corresponding to ≈ 2 to 3 agglomerated C-S-H nanoplates in solution [assuming plate sizes of 60 × 30 × 1.5 nm^3, as determined by transmission electron microscopy (TEM)]. This is further supported by cryo-TEM analysis, where small aggregates of C-S-H particles are observed next to isolated plates (Fig. 1A) in contrast to the sole large aggregates in the absence of polymer (Fig. 1B).

As shown in table S2, the stabilization ability of the copolymers is highly dependent on the pH value of the equilibrium solution and the polymer concentration. Accordingly, two different approaches were designed to trigger and control the aggregation (see the Supplementary Materials and fig. S3): (A) a pH increase from pH 12 to pH 12.8 and (B) an adjustment of the polymer/C-S-H ratio at pH 13. In both cases, C-S-H aggregates in a controlled way and finally settles as mesocrystals after 1 to 3 days. For approach A, time-dependent dynamic light scattering

[1]Physical Chemistry, University of Konstanz, Universitätsstraße 10, 78457 Konstanz, Germany. [2]BASF Construction Solutions GmbH, Advanced Materials and Systems Research, Albert Frank Straße 32, 83304 Trostberg, Germany. [3]Institute for Materials Science, University of Stuttgart, Heisenbergstraße 3, 70569 Stuttgart, Germany. [4]Department of Biomaterials, Max Planck Institute of Colloids and Interfaces, Research Campus Golm, 14424 Potsdam, Germany. [5]ICB (Laboratoire Interdisciplinaire Carnot de Bourgogne), UMR 6303 CNRS, Université de Bourgogne-Franche-Comté, 21078 Dijon Cedex, France.
*Present address: Werderstrasse 20, 69120 Heidelberg, Germany.
†Present address: B CUBE–Center for Molecular Bioengineering, Technische Universität Dresden, 01307 Dresden, Germany.
‡Corresponding author. Email: helmut.coelfen@uni-konstanz.de

measurements revealed that the agglomeration process is not taking place at once but rather occurs via a particle attachment mechanism over a longer period of time (fig. S4).

The obtained structures from both approaches are shown in Fig. 2. Polarized optical microscopy (POM) reveals long-range–oriented C-S-H superstructures (uniform color) on the several hundreds of micrometer scale. Scanning electron microscopy (SEM) shows the alignment of former isolated C-S-H crystallites in defined layered structures. Most notably, the C-S-H superstructures show no pores on the micrometer scale (Fig. 2, B, C, E, and F), which were identified to promote crack propagation and are minimized in MDF cement (*8*). Brunauer-Emmett-Teller (BET) measurements revealed a high inner surface area of 145 m^2/g, which corresponds to a material with an average porosity of 3.9 nm, further supporting the mesocrystal structure (*7*).

The three-dimensional short-range orientation was addressed by means of TEM and selected area electron diffraction (SAED) analysis. A typical SAED pattern of aggregated and pestled C-S-H crystals is shown in Fig. 3A (and in fig. S5). Defined spots are visible and indicate a single crystal–like scattering behavior, whereas single nanoparticles are identified at the edge (Fig. 3B). The radial integration of this pattern corresponds to the powder X-ray diffraction (XRD) pattern of C-S-H (fig. S6), revealing only C-S-H and no salt residues. Powder XRD patterns of the ordered aggregates do not show any peak narrowing compared to the original colloidal C-S-H suspension, indicating

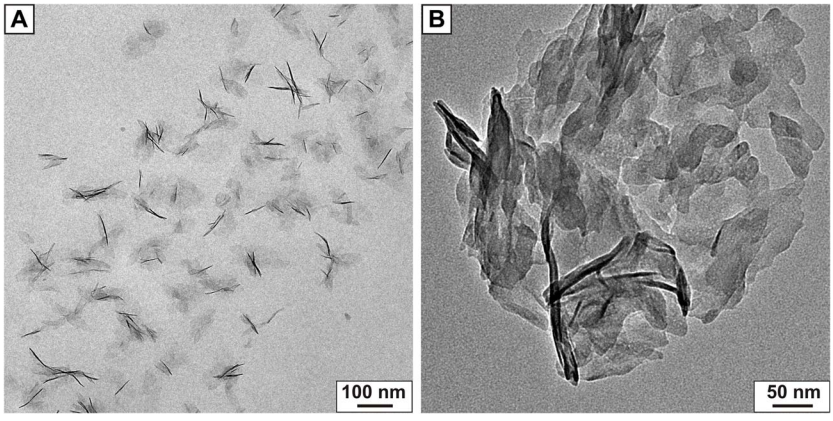

Fig. 1. TEM analysis of C-S-H. (**A**) Cryo-TEM of colloidally stabilized C-S-H crystallites at pH 12 and (**B**) TEM analysis of aggregated C-S-H crystallites in the absence of stabilizing agents. The approximate literature known size of 60 × 30 × 5 nm^3 (*36*) can be assumed in both micrographs.

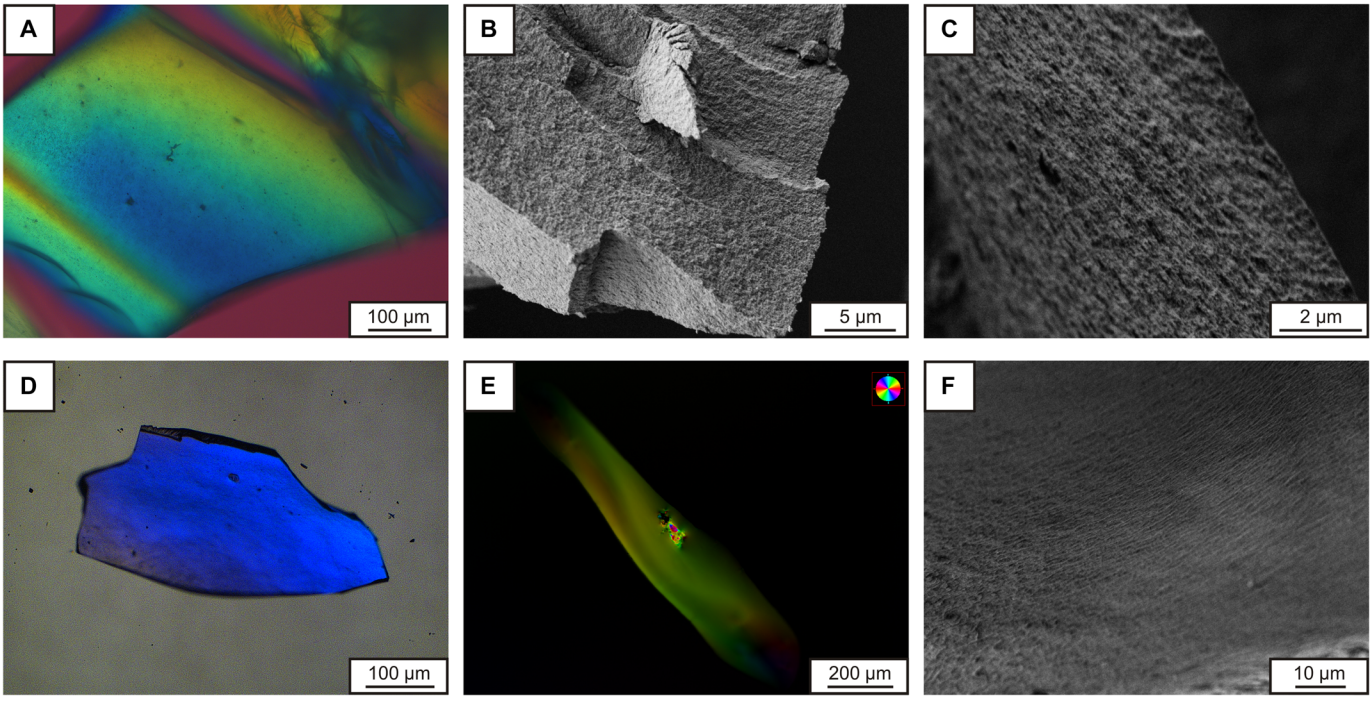

Fig. 2. Polarized optical and scanning electron micrographs of C-S-H mesocrystals. (**A**) to (**C**) were obtained from approach A, and (**D**) to (**F**) from approach B. For (A), (D), and (E), same colors indicate same orientations. The POM analysis suggests a long-range order of the agglomerated C-S-H crystallites over several hundreds of micrometers. (B) reveals a secondary structuring of the C-S-H superstructures, whereas (C) and (F) show the alignment of the single C-S-H crystallites into layers, and no microporosity can be detected.

similar coherent domain sizes (fig. S6). A polymer amount of ≈20 weight % (wt %) and between 5 and 7 wt % was determined for materials obtained from approaches A and B, respectively (fig. S7). These data supported by recent simulations (*18*) suggest that real inorganic-organic hybrids were achieved that can be described as mesocrystals (*11*, *21*) with an organic content ranging between nacre (≈5 wt %) (*22*) and bone (≈35 wt %) (*23*).

Because C-S-H is the main cohesive building block of hydrated cement, the mechanical properties of the C-S-H mesocrystals (approach A) were investigated by means of nanoindentation. The mean reduced modulus and the hardness were determined by indenting two sides of the crystals (parallel and perpendicular to the C-S-H layers), as schematically shown in fig. S8. The obtained values are 9.8 ± 1.4 and 10.4 ± 1.8 GPa for the reduced modulus (Young's modulus of 9.2 and 9.7 GPa, respectively) and 0.40 ± 0.07 and 0.45 ± 0.14 GPa for the hardness, respectively. Both Young's modulus and hardness are lower by ≈60% compared to hydrated cement pastes (*24*). This shows that the polymer C-S-H mesocrystals are more compliant and softer than the common C-S-H assemblage in hydrated cement paste, as visualized in the Ashby plot (fig. S9).

The flexural strength of C-S-H mesocrystals was further evaluated by in situ bending tests of microcantilevers milled from the mesocrystals using a focused ion beam (FIB) microscope. The bending was performed inside a scanning electron microscope using a tungsten needle manipulator. These tests demonstrated large elastic deformations of the C-S-H mesocrystals (Fig. 4 and movie S1), implying strong polymer binding to the C-S-H platelets preventing their irreversible gliding in plastic deformation. Furthermore, the flexural stress, developed in the

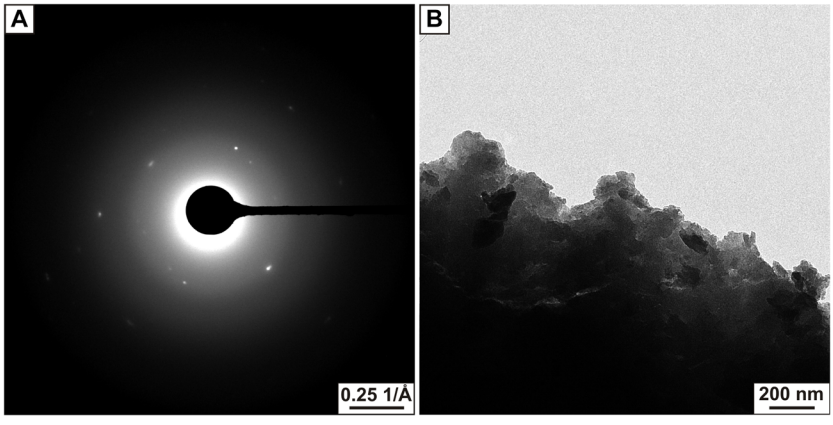

Fig. 3. TEM analysis of the mesocrystals obtained from approach A. (**A**) reveals single crystalline scattering behavior indicating a perfect mutual alignment of the C-S-H nanoparticles in three-dimension (3D). (**B**) shows the existence of single-isolated C-S-H crystallites at the edge. Because the building blocks are not fused together whereas they scatter like single crystals, the obtained agglomerates are mesocrystals.

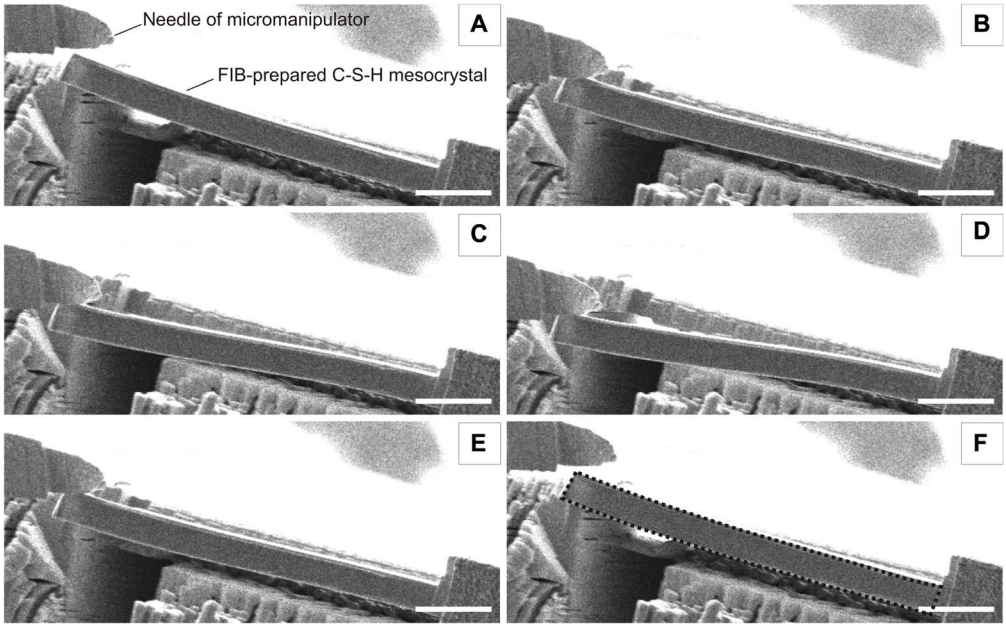

Fig. 4. Visualization of the pronounced flexibility and elasticity of a C-S-H mesocrystal lever prepared by FIB (focused ion beam). (**A**) to (**F**) Picture series of the bending video (available as movie S1) under the scanning electron microscope. The elasticity is revealed because the C-S-H mesocrystal cantilever fully relaxes after the application of a mechanical stress by a micromanipulator (upper left corner). The dashed line in (F) indicates the position of the C-S-H mesocrystal cantilever before bending. Scale bars, 10 μm.

material during bending in the elastic regime, exhibited an impressive value of 153 MPa (see the Supplementary Materials), suggesting that the flexural strength of the C-S-H mesocrystal is even higher, in the ball park of that for nacre (210 MPa) and bovine bone (220 MPa) (*25*), by a factor of 3 higher than that for MDF cement (*8*) and outperforms the flexural strength of regular concrete by a factor of 40 to 100. The comparison demonstrates the advantage of the mesocrystalline order and decreased porosity. Such good performance can be attributed to the tessellated structure and layered arrangement of the nanosized C-S-H particles, along with the strong interparticle polymer connection (*26*), promoting effective load distribution through the mesocrystal, which imparts extraordinary flexibility and strength to the material. In addition, even better performance (162 MPa) was measured when the load is applied parallel to the C-S-H layers (see the Supplementary Materials) similar to the findings reported by Erb *et al.* (*27*).

DISCUSSION

In summary, three-dimensionally ordered C-S-H mesocrystals were synthesized for the first time in solution by a simple self-assembly approach. The tessellated mesocrystal structure combines the stiffness of inorganic C-S-H with the elasticity of polymers, similar to biomaterials such as nacre (*26*). This structure is able to effectively dissipate the energy and withstand flexural stresses of several hundreds of MPa, which are comparable or even higher than those achieved by nacre. The nanometer size of the mineral particles, such as in sea urchin spines (*13*) or bone (*28*), ensures optimum strength and maximum tolerance to flaws (*29*). In addition, the mesocrystal arrangement of C-S-H nanoparticles enables a high packing density of the platelets interspaced with polymer and also optimizes the interactions between the elementary building units. Such a construction strategy was already successful as reported for calcite mesocrystals assembled around a silicatein filament (*30*). However, it is clear that the size of our micromanipulation test shown in Fig. 4 is below that of the components, which are typically added to cement to make up concrete (sands etc.). Therefore, our report shows the maximum of the achievable properties by our approach.

The elaboration of mesocrystals described in this report, starting from the stabilization of C-S-H particles to the controlled agglomeration via a simple pH increase or C-S-H/polymer ratio control, bears a huge potential to be adapted to the real concrete world. With this approach, the elasticity of cementitious materials would begin on the nanoscale, which in turn would dramatically enhance the mechanical properties of future buildings.

MATERIALS AND METHODS

The following chemicals were all used as received: sodium metasilicate (Sigma-Aldrich), calcium chloride (1 M volumetric solution; Fluka), sodium hydroxide (1 M volumetric solution; Merck), poly(1-vinylpyrrolidone-co-acrylic acid) (PVP-co-PAA, 96,000 g/mol; Sigma-Aldrich), and poly (acrylamide-co-acrylic acid) partial sodium salt [PAAm-co-PAA, 200,000 g/mol (≈20 wt % acrylamide, ≈80 wt % acrylic acid); PAAm-co-PAA, 520,000 g/mol (≈80 wt % acrylamide, ≈20 wt % acrylic acid), Sigma-Aldrich].

Syntheses

Colloidal C-S-H

In a typical run, 90 ml of 3.3 mM Na_2SiO_3 was added into an argon-flushed beaker. Ten milliliters of PVP-co-PAA (10 g/liter), PAAm-coPAA (200,000 g/mol), or PAAm-co-PAA (520,000 g/mol) (see fig. S1) polymer stock solution was added, and the pH was adjusted to 12 with 1.5 ml of 1 M NaOH. During the entire synthesis procedure, the solution was showered with water-saturated argon. Then, 35 ml of 30 mM $CaCl_2$ solution was added under stirring at a dosing rate of 0.3 ml/min. After the $CaCl_2$ addition, the solution was stirred for another 12 hours, so that all reactive silicate present in solution precipitated to give colloidal C-S-H with a Ca/Si equal to 1. The solution was then stored in argon-flushed Schlenk flasks until needed for further experiments. Prepared in this way, it stayed stable over several months.

C-S-H mesocrystals

Approach A based on pH increase: The colloidal C-S-H suspension obtained at pH 12 was adjusted to pH 12.8 with 1 M NaOH. After 3 days, the colloidal suspension starts to aggregate and form mesocrystals. Crystals were filtered, washed with H_2O and absolute ethanol, and dried at 40°C. Approach B: 350 mg of PVP-co-PAA was added to 350 ml of 3.3 mM Na_2SiO_3, pH was adjusted to 13 with 100 ml of 1 M NaOH, and the mixture was stirred until a clear solution was obtained. Then, different volumes of 30 mM $CaCl_2$ were added with a constant dosing speed of 0.1 ml/min to give a supersaturation degree $\beta = 28$ (addition of 19 ml of $CaCl_2$) and $\beta = 36$ (addition of 25 ml of $CaCl_2$). After the complete addition of calcium, stirring was stopped, and the obtained solutions were transferred into argon-flushed Schlenk flasks, until precipitation and subsequent agglomeration occurred (1 day for $\beta = 36$ and 2 days for $\beta = 28$). Crystals were filtered, washed with H_2O and absolute ethanol, and dried at 40°C.

Analysis

For the TEM specimen preparation, a small aliquot of the C-S-H dispersion was transferred on a copper formvar/carbon grid in argon atmosphere by blotting with a filter paper. The C-S-H crystals were pestled, dispersed in absolute ethanol, and blotted onto a TEM grid. The TEM used was a Zeiss Libra 120, which operates with a 120-kV LaB_6 emitter with Koehler illumination and a resolution of 0.34 nm.

For cryo-TEM, an aliquot of the colloidal solution was spread on a lacey carbon grid by blotting with a filter paper. The resulting thin film was vitrified by quickly plunging the grid into liquid ethane at its freezing point. Specimens were examined at temperatures around 90 K. Collected images were processed with a background subtraction routine, and where appropriate, a smoothing filter was applied to reduce noise. The measurements were performed at the University of Bayreuth with a Zeiss EM922 EF microscope, operated at 200 kV, and equipped with a Gatan CT3500 cryo-transfer holder. Images were acquired with a Gatan UltraScan US 1000 high-resolution cooled charge-coupled device camera and processed using the Digital Micrograph Suite 1.8 software package.

Long-range ordering of C-S-H mesocrystals was studied with a light microscope (Zeiss Axio Imager M2m), equipped with four different objectives (10×/0.2 pol, 20×/0.5 pol, 50×/0.8 pol, and 100×/0.9 pol) and the corresponding polarizers with lambda filters. The microscope was additionally equipped with an Abrio imaging system (CRi Inc.). The SEM analysis was performed with a Zeiss Gemini ultrahigh resolution field-emission SEM with a resolution of 2.5 nm at 1 kV.

For nanoindentation, mesocrystals obtained from approach A were embedded into poly(methyl methacrylate) (PMMA) and then polished with suspended diamond particles down to a particle size of 0.25 μm to obtain a relatively smooth surface. Then, experiments were performed with 30 indentations perpendicular to the layered structure and 35 indentations parallel to the layered structure. In all indentation tests, a loading function, consisting of 5 s of loading—30-s holding under

maximal load— and 5 s of unloading with a maximal applied load of 500 μN, was chosen. The maximum penetration depth reached during the measurements was 500 nm. Young's modulus was then calculated according to Eq. 1. The value for the elastic modulus and Poisson's ratio of the diamond tip was set to 1141 GPa and 0.07, respectively, and a Poisson's ratio for C-S-H (0.27) was extracted from Helmuth *et al.* (*31*). The nanoindenter used was a Hysitron Triboindenter TI950 equipped with a Berkovich tip located at the Max Planck Institute of Colloids and Interfaces in Golm, Germany. The reduced modulus from nanoindentation measurements was converted into Young's modulus using

$$E = \frac{1 - \nu^2}{\frac{1}{E_r} - \frac{1-\nu_i^2}{E_i}} \quad (1)$$

where E_i, E, ν_i, and ν are the elastic moduli and Poisson ratio of the indenter (indexed with i) and the material, respectively. E_r is the measured reduced modulus.

For the bending tests on the mesocrystals from approach A, cantilever beams were prepared by Ga ion beam milling using a Zeiss Crossbeam 15 EsB instrument operated at an ion acceleration voltage of 30 kV and incident beam currents of 10 nA to 100 pA. Final polishing was performed using the low ion current of 100 pA to minimize surface damage. The cantilever beam was cut from the bulk material such that its long axis is parallel to the layers of the C-S-H mesocrystal–polymer hybrid. The cantilever dimensions of 44.84-μm length × 3.2-μm width × 3.68-μm thickness were chosen to ensure that the cantilever length is more than 10 times larger than its width. The cantilever thickness had to be above 3 μm to avoid pronounced bending after the last cutting step. As apparent from fig. S10, one end of the cantilever remained attached to the sample, without the need for a separate fixing point.

The bending tests were performed with the aid of a Kleindiek (Reutlingen) MM3a micromanipulator equipped with a fine tungsten needle. The cantilever was subjected to several cycles of loading and complete unloading, with the load, applied by the tungsten needle, being perpendicular to the C-S-H layers in the sample (fig. S10C). In our experiments, the load applied by the tungsten needle, necessary for bending the sample, is not directly known. However, it can be calculated using the classical Timoshenko beam theory (Eq. 2) combined with the Young's modulus of the cantilever, which was determined by the nanoindentation tests (*32*). Hence, the Young's modulus in the direction parallel to the crystal layers is needed to calculate the load because the bending of the cantilever occurs perpendicular to the crystal layers and vice versa. In accordance with the beam bending theory, and assuming that the measurement is performed in a pure linear elastic regime, the applied load (P) can be calculated from the Young's modulus (E), the displacement (δ), and the cantilever geometry using Eq. 2 (*33*)

$$E = \frac{P}{\delta}\frac{4L^3}{le^3} \quad (2)$$

where e is the thickness, l is the width, and L is the length (distance from the point of attachment A to contact point with needle B) of the cantilever, respectively, as illustrated in fig. S11. Note that Eq. 2 holds only for small beam deflections (δ << L) (*34*, *35*). The actual dimensions of the cantilever used in the bending experiments are presented in fig. S12.

The load required for bending the cantilever up to a displacement of 5.1 μm is calculated to be approximately 29 μN, which is a reasonable value for a sample of such a size (*34*). The maximal flexural stress during bending of the cantilever material is accessible via Eq. 3, which describes the maximal stress in the cantilever, at the fixed end of the beam where the applied moment is the highest (point "A" in fig. S11)

$$\sigma = \frac{6\,PL}{le^2} \quad (3)$$

To determine the influence of crystal orientation on the flexural strength, the same procedure was repeated with the applied load parallel to the crystal layer planes (fig. S13). The cantilever dimensions were 33.88-μm length × 2.16-μm width × 2.55-μm thickness. Data evaluation for the bending displacement of 5 μm, similar to the cantilever with perpendicular crystal layers, revealed that the maximal flexural stress (162 MPa) is even higher. Displacement of 5 μm was chosen to ensure that the deformation occurs within an elastic regime, as it is shown in movies S1 and S2, where cantilever deformation was fully reversible. Moreover, maximum displacements of 6.25 and 8.00 μm were possible for cantilevers with perpendicular and parallel crystal orientation, respectively, before breaking. For this displacement, even higher flexural stresses were calculated (198 and 258 MPa, respectively). However, in this case, it is highly possible that the deformation exceeded the elastic regime and Eq. 3 is no longer valid.

These flexural stresses are by far higher than the flexural strength even of a fiber-reinforced ultrahigh performance concrete of 50 MPa (*7*) or an MDF cement of 60 to 70 MPa (*8*, *9*) and almost as high as that of nacre (210 MPa) (*25*). An attempt was made to perform a similar bending experiment with a pure C-S-H reference, but this experiment failed because pure C-S-H was too brittle. This can be attributed to the porosity of C-S-H, and an ideally packed C-S-H phase should have an indentation modulus of 61.2 GPa and a hardness of 1.78 GPa as extrapolated by Constantinides using nanoindentation experiments (*24*). This is much higher than the approximately 10-GPa Young's modulus and 0.4-GPa hardness measured for the C-S-H, respectively.

SUPPLEMENTARY MATERIALS

Supplementary material for this article is available at http://advances.sciencemag.org/cgi/content/full/3/11/e1701216/DC1

table S1. Mechanical properties of nacre and typical nacre-like layered nanocomposites.
table S2. Colloidal stability of C-S-H in the presence of different copolymers at various conditions.
fig. S1. Chemical structures of C-S-H stabilizing polymers.
fig. S2. AUC measurements of PVP-co-PAA–stabilized C-S-H nanoplates.
fig. S3. Strategy for the formation of nanostructured hybrid C-S-H.
fig. S4. Dynamic light scattering of growing C-S-H mesocrystals.
fig. S5. Evaluation of the mesocrystalline domain sizes of self-assembled C-S-H crystals (approach A).
fig. S6. Wide-angle x-ray pattern of filtered polymer-stabilized C-S-H nanoplates (red curve) and obtained mesocrystals from pH increase (approach A, black curve) compared to C-S-H from pozzolanic reaction with CaO and SiO2 (Ca/Si = 1) (green curve).
fig. S7. Thermogravimetric analysis of C-S-H mesocrystals.
fig. S8. Schematical illustration of the two differently performed nanoindentation experiments on C-S-H mesocrystals from approach A.
fig. S9. Ashby plot comparing the mechanical properties of the C-S-H mesocrystals (approach A) with various materials.
fig. S10. SEM images of a cantilever beam used in the bending tests with the applied load perpendicular to the crystal layer planes.
fig. S11. Schematic illustration of in-situ bending experiments.
fig. S12. Dimensions of a cantilever beam used in the bending tests with the load applied perpendicular to the crystal layers.
fig. S13. SEM images of a cantilever beam used in the bending tests with the load applied parallel to the crystal layers.
movie S1. Bending test of mesocrystals obtained from pH increase to pH 12.8 under the scanning electron microscope.

movie S2. Bending test of the same mesocrystals such as in movie S1 except that the applied stress is parallel to the crystal layer planes.
References (*37*–*49*)

REFERENCES AND NOTES

1. A. M. Neville, *Properties of Concrete* (Pitman, 1963).
2. H. Matsuyama, J. F. Young, Intercalation of polymers in calcium silicate hydrate: A new synthetic approach to biocomposites? *Chem. Mater.* **11**, 16–19 (1999).
3. J. Minet, S. Abramson, B. Bresson, C. Sanchez, V. Montouillout, N. Lequeux, New layered calcium organosilicate hybrids with covalently linked organic functionalities. *Chem. Mater.* **16**, 3955–3962 (2004).
4. F. Merlin, H. Lombois, S. Joly, N. Lequeux, J.-L. Halary, H. Van Damme, Cement-polymer and clay-polymer nano- and meso-composites: Spotting the difference. *J. Mater. Chem.* **12**, 3308–3315 (2002).
5. F. Pelisser, P. J. P. Gleize, A. Mikowski, Effect of poly(diallyldimethylammonium chloride) on nanostructure and mechanical properties of calcium silicate hydrate. *Mater. Sci. Eng. A* **527**, 7045–7049 (2010).
6. J. Rieger, M. Kellermeier, L. Nicoleau, Formation of nanoparticles and nanostructures—An industrial perspective on $CaCO_3$, cement, and polymers. *Angew. Chem. Int. Ed. Engl.* **53**, 12380–12396 (2014).
7. D. J. Kim, S. H. Park, G. S. Ryu, K. T. Koh, Comparative flexural behavior of hybrid ultra high performance fiber reinforced concrete with different macro fibers. *Construct. Build Mater.* **25**, 4144–4155 (2011).
8. J. D. Birchall, A. J. Howard, K. Kendall, Flexural strength and porosity of cements. *Nature* **289**, 388–390 (1981).
9. J. D. Birchall, A. J. Howard, K. Kendall, A cement spring. *J. Mater. Sci. Lett.* **1**, 125–126 (1982).
10. R. O. Ritchie, The conflicts between strength and toughness. *Nat. Mater.* **10**, 817–822 (2011).
11. L. Bergström, E. V. Sturm née Rosseeva, G. Salazar-Alvarez, H. Cölfen, Mesocrystals in biominerals and colloidal arrays. *Acc. Chem. Res.* **48**, 1391–1402 (2015).
12. Y. Oaki, A. Kotachi, T. Miura, H. Imai, Bridged nanocrystals in biominerals and their biomimetics: Classical yet modern crystal growth on the nanoscale. *Adv. Funct. Mater.* **16**, 1633–1639 (2006).
13. J. Seto, Y. Ma, S. A. Davis, F. Meldrum, A. Gourrier, Y.-Y. Kim, U. Schilde, M. Sztucki, M. Burghammer, S. Maltsev, C. Jäger, H. Cölfen, Structure-property relationships of a biological mesocrystal in the adult sea urchin spine. *Proc. Natl. Acad. Sci.* **109**, 3699–3704 (2012).
14. A. Picker, L. Nicoleau, A. Nonat, C. Labbez, H. Cölfen, Identification of binding peptides on calcium silicate hydrate: A novel view on cement additives. *Adv. Mater.* **26**, 1135–1140 (2014).
15. M. Delhorme, C. Labbez, M. Turesson, E. Lesniewska, C. E. Woodward, B. Jönsson, Aggregation of calcium silicate hydrate nanoplatelets. *Langmuir* **32**, 2058–2066 (2016).
16. C. Labbez, B. Jönsson, C. Woodward, A. Nonat, M. Delhorme, The growth of charged platelets. *Phys. Chem. Chem. Phys.* **16**, 23800–23808 (2014).
17. L. Nicoleau, T. Gädt, L. Chitu, G. Maier, O. Paris, Oriented aggregation of calcium silicate hydrate platelets by the use of comb-like copolymers. *Soft Matter* **9**, 4864–4874 (2013).
18. M. Turesson, A. Nonat, C. Labbez, Stability of negatively charged platelets in calcium-rich anionic copolymer solutions. *Langmuir* **30**, 6713–6720 (2014).
19. M. Turesson, C. Labbez, A. Nonat, Calcium mediated polyelectrolyte adsorption on like-charged surfaces. *Langmuir* **27**, 13572–13581 (2011).
20. D. Gebauer, A. Völkel, H. Cölfen, Stable prenucleation calcium carbonate clusters. *Science* **322**, 1819–1822 (2008).
21. H. Cölfen, M. Antonietti, *Mesocrystals and Nonclassical Crystallization* (John Wiley & Sons, 2008).
22. I. Corni, T. J. Harvey, J. A. Wharton, K. R. Stokes, F. C. Walsh, R. J. K. Wood, A review of experimental techniques to produce a nacre-like structure. *Bioinspir. Biomim.* **7**, 031001 (2012).
23. P. A. Downey, M. I. Siegel, Bone biology and the clinical implications for osteoporosis. *Phys. Ther.* **86**, 77–91 (2006).
24. G. Constantinides, F.-J. Ulm, The nanogranular nature of C–S–H. *J. Mech. Phys. Solids* **55**, 64–90 (2007).
25. J. D. Currey, P. Zioupos, P. Davies, A. Casinos, Mechanical properties of nacre and highly mineralized bone. *Proc. Biol. Sci.* **268**, 107–111 (2001).
26. P. Fratzl, O. Kolednik, F. D. Fischer, M. N. Dean, The mechanics of tessellations – bioinspired strategies for fracture resistance. *Chem. Soc. Rev.* **45**, 252–267 (2016).
27. R. M. Erb, R. Libanori, N. Rothfuchs, A. R. Studart, Composites reinforced in three dimensions by using low magnetic fields. *Science* **335**, 199–204 (2012).
28. S. Weiner, H. D. Wagner, The material bone: Structure-mechanical function relations. *Annu. Rev. Mater. Sci.* **28**, 271–298 (1998).
29. H. Gao, B. Ji, I. L. Jäger, E. Arzt, P. Fratzl, Materials become insensitive to flaws at nanoscale: Lessons from nature. *Proc. Natl. Acad. Sci.* **100**, 5597–5600 (2003).
30. F. Natalio, T. P. Corrales, M. Panthöfer, D. Schollmeyer, I. Lieberwirth, W. E. G. Müller, M. Kappl, H.-J. Butt, W. Tremel, Flexible minerals: Self-assembled calcite spicules with extreme bending strength. *Science* **339**, 1298–1302 (2013).
31. R. A. Helmuth, D. H. Turk, The reversible and irreversible drying shrinkage of hardened portland cement and tricalcium silicate pastes. *J. PCA. Res. Dev. Lab.* **9**, 8–21 (1967).
32. M. D. Diop, in *Nanoindentation in Materials Science,* J. Nemecek, Ed. (InTech, 2012), chap. 9, pp. 205–228.
33. J. M. Gere, S. P. Timoshenko, *Mechanics of Materials* (Van Nostrand, 1972).
34. T. P. Weihs, S. Hong, J. C. Bravman, W. D. Nix, Mechanical deflection of cantilever microbeams: A new technique for testing the mechanical properties of thin films. *J. Mater. Res.* **3**, 931–942 (1988).
35. D. Son, J.-h. Jeong, D. Kwon, Film-thickness considerations in microcantilever-beam test in measuring mechanical properties of metal thin film. *Thin Solid Films* **437**, 182–187 (2003).
36. A. Nonat, The structure and stoichiometry of C-S-H. *Cem. Concr. Res.* **34**, 1521–1528 (2004).
37. M. Sarikaya, An introduction to biomimetics: A structural viewpoint. *Microsc. Res. Tech.* **27**, 360–375 (1994).
38. Z. Y. Tang, N. A. Kotov, S. Magonov, B. Ozturk, Nanostructured artificial nacre. *Nat. Mater.* **2**, 413–418 (2003).
39. P. Podsiadlo, Z. Tang, B. S. Shim, N. A. Kotov, Counterintuitive effect of molecular strength and role of molecular rigidity on mechanical properties of layer-by-layer assembled nanocomposites. *Nano Lett.* **7**, 1224–1231 (2007).
40. P. Podsiadlo, A. K. Kaushik, E. M. Arruda, A. M. Waas, B. S. Shim, J. Xu, H. Nandivada, B. G. Pumplin, J. Lahann, A. Ramamoorthy, N. A. Kotov, Ultrastrong and stiff layered polymer nanocomposites. *Science* **318**, 80–83 (2007).
41. P. Podsiadlo, A. K. Kaushik, B. S. Shim, A. Agarwal, Z. Tang, A. M. Waas, E. M. Arruda, N. A. Kotov, Can nature's design be improved upon? High strength, transparent nacre-like nanocomposites with double network of sacrificial cross links. *J. Phys. Chem. B* **112**, 14359–14363 (2008).
42. T.-H. Lin, W.-H. Huang, I.-K. Jun, P. Jiang, Bioinspired assembly of colloidal nanoplatelets by electric field. *Chem. Mater.* **21**, 2039–2044 (2009).
43. E. Munch, M. E. Launey, D. H. Alsem, E. Saiz, A. P. Tomsia, R. O. Ritchie, Tough, bio-inspired hybrid materials. *Science* **322**, 1516–1520 (2008).
44. H.-B. Yao, Z.-H. Tan, H.-Y. Fang, S.-H. Yu, Artificial nacre-like bionanocomposite films from the self-assembly of chitosan-montmorillonite hybrid building blocks. *Angew. Chem. Int. Ed. Engl.* **49**, 10127–10131 (2010).
45. A. Finnemore, P. Cunha, T. Shean, S. Vignolini, S. Guldin, M. Oyen, U. Steiner, Biomimetic layer-by-layer assembly of artificial nacre. *Nat. Commun.* **3**, 966 (2012).
46. L.-P. Xu, J. Peng, Y. Liu, Y. Wen, X. Zhang, L. Jiang, S. Wang, Nacre-inspired design of mechanical stable coating with underwater superoleophobicity. *ACS Nano* **7**, 5077–5083 (2013).
47. P. Das, S. Schipmann, J.-M. Malho, B. Zhu, U. Klemradt, A. Walther, Facile access to large-scale, self-assembled, nacre-inspired, high-performance materials with tunable nanoscale periodicities. *ACS Appl. Mater. Interfaces* **5**, 3738–3747 (2013).
48. X. Hu, Z. Xu, Z. Liu, C. Gao, Liquid crystal self-templating approach to ultrastrong and tough biomimic composites. *Sci. Rep.* **3**, 2374 (2013).
49. H. F. W. Taylor, *Cement Chemistry* (Thomas Telford, ed. 2, 1997).

Acknowledgments: We thank M. Siglreitmeier, M. Kellermeier, and M. Drechsler for the electron microscopy, B. Fenk for the FIB preparation and bending tests, as well as the service group of J. Weis from the Max Planck Institute (MPI) in Stuttgart for the support and equipment access. We would also like to thank A. Knöller for the helpful comments in the editing of this manuscript. H.C. claims responsibility for all the figures in the main text and Supplementary Materials. **Funding:** This work was funded by BASF Construction Solutions GmbH. **Author contributions:** H.C. and L.N. designed the project. A.P. synthesized the materials and performed most of the analyses. Z.B. and I.Z. performed the mechanical measurements. C.L., A.N., and J.B. contributed to the discussions of all the results. H.C. and A.P. wrote the manuscript with contributions from all the other authors. **Competing interests:** The authors declare that they have no competing interests. **Data and materials availability:** All data needed to evaluate the conclusions in the paper are present in the paper and/or the Supplementary Materials. Additional data related to this paper may be requested from the authors.

Submitted 17 April 2017
Accepted 19 October 2017
Published 29 November 2017
10.1126/sciadv.1701216

Citation: A. Picker, L. Nicoleau, Z. Burghard, J. Bill, I. Zlotnikov, C. Labbez, A. Nonat, H. Cölfen, Mesocrystalline calcium silicate hydrate: A bioinspired route toward elastic concrete materials. *Sci. Adv.* **3**, e1701216 (2017).

Mesocrystalline calcium silicate hydrate: A bioinspired route toward elastic concrete materials

Andreas Picker, Luc Nicoleau, Zaklina Burghard, Joachim Bill, Igor Zlotnikov, Christophe Labbez, André Nonat and Helmut Cölfen

Sci Adv **3** (11), e1701216.
DOI: 10.1126/sciadv.1701216